

Study of the performance of a novel 1 mm resolution dual-panel PET camera design dedicated to breast cancer imaging using Monte Carlo simulation

Jin Zhang,^{a)} Peter D. Olcott,^{b)} Garry Chinn,^{c)} Angela M. K. Foudray,^{d)} and Craig S. Levin^{e)}
Department of Radiology and Molecular Imaging Program, Stanford University, Stanford, California 94305

(Received 31 January 2006; revised 25 September 2006; accepted for publication 21 November 2006; published 26 January 2007)

We studied the performance of a dual-panel positron emission tomography (PET) camera dedicated to breast cancer imaging using Monte Carlo simulation. The PET camera under development has two $10 \times 15 \text{ cm}^2$ plates that are constructed from arrays of $1 \times 1 \times 3 \text{ mm}^3$ LSO crystals coupled to novel ultra-thin ($<200 \mu\text{m}$) silicon position-sensitive avalanche photodiodes (PSAPD). In this design the photodetectors are configured “edge-on” with respect to incoming photons which encounter a minimum of 2 cm thick of LSO with directly measured photon interaction depth. Simulations predict that this camera will have 10–15% photon sensitivity, for an 8–4 cm panel separation. Detector measurements show $\sim 1 \text{ mm}^3$ intrinsic spatial resolution, $<12\%$ energy resolution, and $\sim 2 \text{ ns}$ coincidence time resolution. By performing simulated dual-panel PET studies using a phantom comprising active breast, heart, and torso tissue, count performance was studied as a function of coincident time and energy windows. We also studied visualization of hot spheres of 2.5–4.0 mm diameter and various locations within the simulated breast tissue for $1 \times 1 \times 3 \text{ mm}^3$, $2 \times 2 \times 10 \text{ mm}^3$, $3 \times 3 \times 30 \text{ mm}^3$, and $4 \times 4 \times 20 \text{ mm}^3$ LSO crystal resolutions and different panel separations. Images were reconstructed by focal plane tomography with attenuation and normalization corrections applied. Simulation results indicate that with an activity concentration ratio of tumor:breast:heart:torso of 10:1:10:1 and 30 s of acquisition time, only the dual-plate PET camera comprising $1 \times 1 \times 3 \text{ mm}^3$ crystals could resolve 2.5 mm diameter spheres with an average peak-to-valley ratio of 1.3. © 2007 American Association of Physicists in Medicine.
[DOI: [10.1118/1.2409480](https://doi.org/10.1118/1.2409480)]

I. INTRODUCTION

Currently, there are certain challenges associated with the detection, diagnosis, and staging of breast cancer. Mammography is accepted as the best means to screen for nonpalpable breast cancer. However, $\sim 30\%$ of screened cases are inconclusive due to radio-dense or distorted breast tissue. The non-specific nature of the structural signatures (microcalcifications and masses) for breast cancer determined by mammography results in a very high false positive rate ($\sim 70\text{--}80\%$);¹ and approximately 600 000 unnecessary biopsies (at $\$1\text{--}3 \text{ K}$ per procedure) are performed annually in the U.S. Standard imaging techniques such as ultrasound and digital x ray to guide biopsy often result in sampling errors of neoplastic tissues. Practical functional imaging methods to guide biopsy are needed to help improve diagnostic accuracy. Biopsy itself causes scarring, which can cause difficulties in the interpretation of future mammograms. Staging breast cancer through axillary lymph node dissection causes significant trauma, including lymphedema and it would be desirable to reduce the degree of invasiveness of this procedure, especially for cases where lymphatic involvement is unlikely. There is also no efficient method to evaluate efficacy of novel breast cancer treatments and/or monitor local recurrence after surgery. Clearly a more specific, sensitive, and noninvasive technique is needed to assist with these pitfalls in breast cancer management.

Positron emission tomography (PET) is a noninvasive, *in vivo*, molecular, and cellular imaging technology. PET has shown promise for more specific identification of cancer due to its unique ability to sense and visualize increased biochemical and molecular changes in malignant compared to healthy tissue. This additional information is useful since cellular changes associated with cancer can occur well before structural changes, such as calcifications, are evident.² However, PET has not been incorporated into standard practice for breast cancer patient evaluation due to: (1) The lack of tracers with adequate specificity; (2) awkward, low coincidence photon detection efficiency (“photon sensitivity”) geometry for breast imaging; (3) relatively long scan times; (4) nonoptimal spatial and energy resolutions for early breast cancer identification; and (5) relatively high cost per study. We are developing a compact, high performance breast-dedicated PET system to address the last four issues and guide the development of new tracers that will address the first issue. Just as a dedicated system (mammography) is required to optimize x-ray breast imaging, the authors and others^{3–7} argue that a dedicated camera is crucial to optimize PET breast imaging, and without such a system, we are far from reaching PET’s potential to play a role in breast cancer management. If successful, such a camera will have impact on increasing the role of PET in breast cancer patient evaluation.

The proposed system will be configured into a compact system dedicated to close-proximity, breast and/or axillary node imaging with high photon sensitivity, 3D positioning capabilities and ultra-high spatial, energy, and coincident time resolutions. If used in conjunction with a highly specific breast cancer tracer, this high photon sensitivity, high resolution imaging system would facilitate significantly more accurate identification of developing, spreading or recurring breast cancer. Using a tracer with nonspecific uptake (e.g., fluorodeoxyglucose), there will likely be background activity generated from the nearby heart and liver. Excellent energy and time resolutions and flexible positioning of a breast-dedicated camera will help to reduce the resulting high background scatter and random coincidence rates that can degrade lesion contrast resolution. As is true for mammography, imaging the chest wall at close proximity is challenging. However, the proposed dual-panel geometry may be opened wider and oriented favorably to contain the chest wall. Finally, for the long term, a small, relatively inexpensive camera dedicated to breast imaging could significantly reduce costs of the technique to the point that it becomes cost-effective for a variety of breast cancer indications. The amount of scintillator required for a breast-dedicated camera is an order of magnitude lower than that present in clinical PET systems. The system will use avalanche photodiodes (APD) as photodetectors rather than photomultiplier tubes (PMT). The long term pricing goal of APDs is \$3–10 per channel, assuming a more widespread use, which is an order of magnitude cheaper than PMTs. Thus, a future goal is that in production, the proposed system would be an order of magnitude cheaper than a standard clinical PET system. We hypothesize that a low system cost is one of the key factors for PET to play a larger role in breast cancer management. A desired outcome is a PET breast imaging exam cost that is determined by the breast cancer radiotracer, rather than the imaging system.

Our hypothesis is that a high performance, compact, cost-effective design dedicated to close-proximity breast imaging, that can rapidly form images with highly specific tracers would help increase the role of PET imaging in the management of breast cancer. Such an imaging system would complement standard methods used for breast cancer screening, diagnosis, and staging. Although at this point the device is experimental, there are several potential indications for this camera that are envisioned: (1) Evaluate a patient for breast cancer when mammography is inconclusive, (2) visualize certain miniscule malignant lesions in earlier stages of growth; (3) for mammography positive lesions, the system can help guide biopsy using a fine needle labeled with a positron emitter. (Others have proposed imaging methods to guide biopsy.^{8–16}); (4) avoid, limit, or guide more extensive surgical procedures associated with breast cancer diagnosis and staging; (5) monitor the patient locally (e.g., evaluate tumor margins) during surgical interventions or their response after novel therapies or treatments are introduced.

A number of other breast-dedicated PET designs are under development.^{3–7} These designs allow closer proximity imaging of breast tissue for improved performance and are

generally based on position-sensitive photomultiplier tubes (PSPMT) and 2 to 3 mm scintillation crystal pixel size. These camera systems as well as standard PET systems¹⁷ have demonstrated spatial resolutions of approximately 2.5–5 mm full width at half maximum (FWHM)^{3–7,17} at the center of the system field of view (FOV), which degrades as a function of position from the center. To push the performance limits further, we are developing a different breast-dedicated PET camera based on 1 mm lutetium oxyorthosilicate (LSO) crystals coupled to novel thin (<200 μm) semiconductor photodetectors known as position sensitive avalanche photodiodes (PSAPD) that are available from RMD, Inc. (Watertown, MA). The goal of this new system is to achieve ~ 1 mm intrinsic spatial resolution uniformly throughout the FOV, >10% photon sensitivity for a point source at the center of the FOV, and excellent energy and temporal resolutions in order to achieve high contrast resolution. The detectors comprise arrays of LSO crystals coupled side-ways to PSAPDs for >90% scintillation light collection efficiency,¹⁸ and directly measured photon depth-of-interaction (DOI) in effectively 2 cm thick LSO crystals. Preliminary experimental results with a standard PSAPD packaged on ceramic substrate¹⁹ as well as the new thin PSAPD²⁰ have been reported. The proposed detector design achieved ~ 1 mm FWHM intrinsic spatial resolution, 3 mm FWHM DOI resolution, <12% FWHM energy resolution at 511 keV, and ~ 2 ns FWHM coincidence time resolution.²⁰

In this paper, we present results of Monte Carlo simulation studies of photon sensitivity, coincidence count rates, and lesion visualization capabilities of the proposed dual-panel PET camera design. To understand the need for 1 mm spatial resolution, we also present a comparison of lesion visualization capabilities for detector panels based on different LSO crystal sizes of $2 \times 2 \times 10 \text{ mm}^3$, $3 \times 3 \times 30 \text{ mm}^3$, and $4 \times 4 \times 20 \text{ mm}^3$. The $2 \times 2 \times 10 \text{ mm}^3$ and $3 \times 3 \times 30 \text{ mm}^3$ crystal dimensions correspond to that used in existing dedicated breast PET system designs studied by other groups. The $4 \times 4 \times 20 \text{ mm}^3$ LSO crystal dimension is used in standard clinical whole body PET systems.¹⁷ Although we are developing iterative image reconstructions for this dual-panel system, in this paper images were reconstructed with a focal plane tomography (FPT) algorithm.

II. MATERIALS AND METHODS

We used GATE (Geant4 Application in Tomographic Emission) open source software²¹ to perform the Monte Carlo simulations on the dual-panel PET camera. Figure 1 depicts the geometry of the simulated dual-plate PET system [Fig. 1(a)], detector module design [Fig. 1(b)], an individual scintillation detector layer [Fig. 1(c)], and a measured energy spectrum with the detector [Fig. 1(d)]. The simulated camera comprises two $10.01 \times 15.4 \times 2.2 \text{ cm}^3$ panels [Fig. 1(a)] with effectively 2.0 cm thick LSO crystals. The camera panel size of $10 \times 15 \text{ cm}^2$ is the minimum FOV that the breast radiologist felt would be useful to be able to image the breast and axillary lymph nodes. If the current design is successful, a later version of the camera will be larger to match the size of

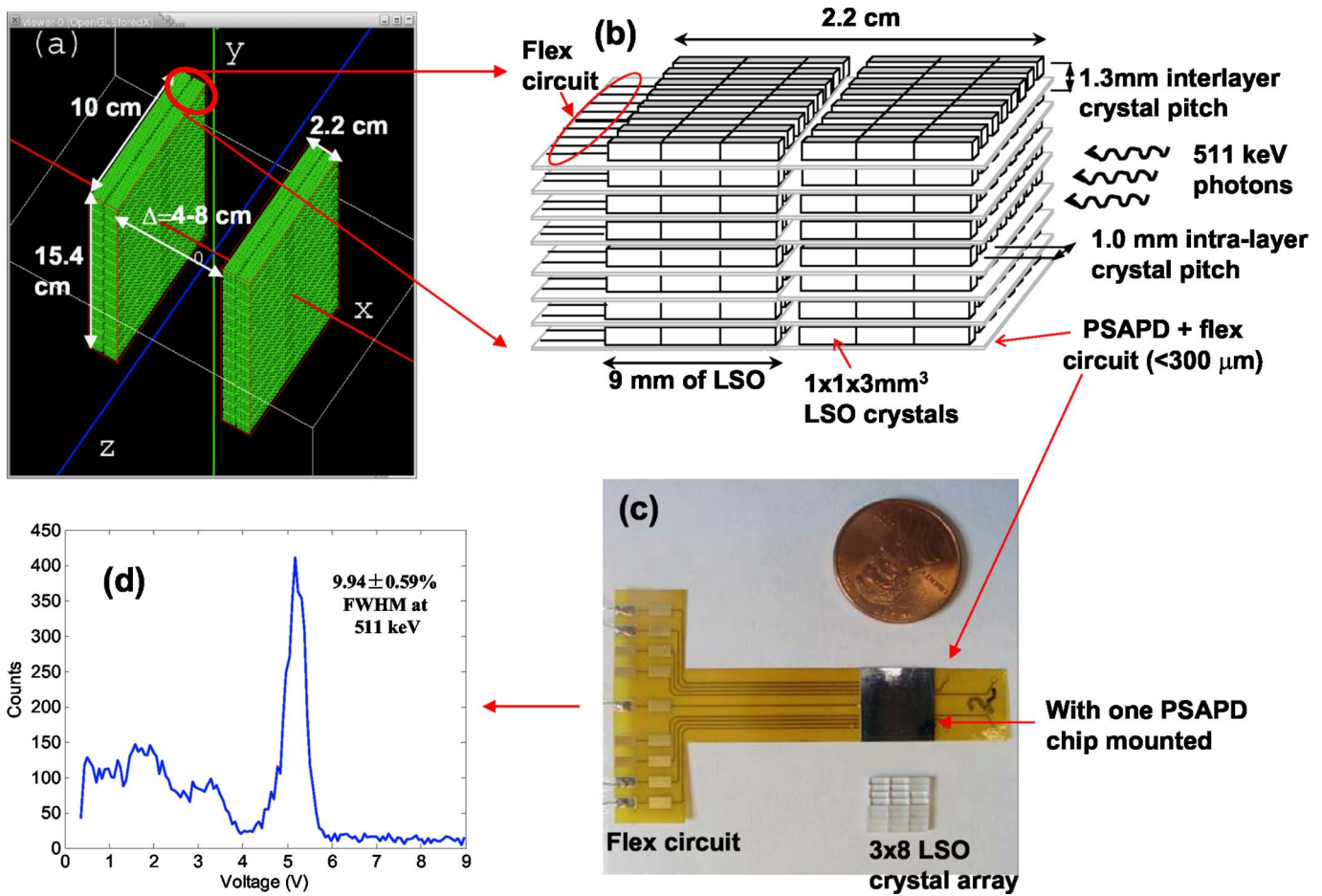


FIG. 1. (a) Dual-panel PET camera geometry based on the novel thin PSAPD. (b) Schematic of a block detector module. (c) Picture of an 8×3 array of $1 \times 1 \times 3 \text{ mm}^3$ LSO crystals and a thin PSAPD chip mounted directly on a Kapton flex circuit. The device (PSAPD chip+flex circuit) is ~ 250 microns thick. Although just one PSAPD chip is mounted on the flex device shown in the picture two chips will be mounted onto the same flex cable. (d) The best ^{22}Na (511 keV photon) energy spectrum measured in one of the LSO array crystals coupled to the PSAPD in (c).

mammography panels. Each panel comprises scintillation detector sub-modules built from layers of LSO crystal arrays coupled to PSAPDs [Fig. 1(b)]. Each scintillation detector layer comprises two 3×8 arrays of $1 \times 1 \times 3 \text{ mm}^3$ LSO crystals with no inter-crystal gaps coupled to two $11 \times 11 \text{ mm}^2$ PSAPD chips [Fig. 1(c)]. The 2.2 cm dimension of the system corresponds to the width of two PSAPD chips [Fig. 1(c)] to which the crystal array is coupled. This configuration provides a total of six crystal layers (each 3 mm thick) for photon interaction depth measurement. The $11 \times 11 \text{ mm}^2$ PSAPD chips have $8 \times 8 \text{ mm}^2$ sensitive area with $\sim 200 \mu\text{m}$ thickness and are mounted to $50 \mu\text{m}$ thick Kapton flex circuits [Fig. 1(c)]. Each scintillation crystal layer requires a ~ 50 micron thick reflector layer. This yields an overall scintillation crystal packing fraction for the two detector panels of approximately 56% (44% dead area), which includes all inter- and intra-module dead gaps. All inter-layer and inter-module dead regions are included in the simulated system model. The detector panel separation is adjustable and 4–8 cm separation was studied in this paper. Figure 1(d) shows the best energy spectrum measured for one of the $1 \times 1 \times 3 \text{ mm}^3$ LSO crystals in the 3×8 array coupled to the thin PSAPD ($9.94 \pm 0.59\%$ FWHM at 511 keV). The average

measured energy and coincidence time resolutions for crystals coupled to the sensitive area of the PSAPD was $<12\%$ and $\sim 2 \text{ ns}$ FWHM, respectively.²⁰

For the photon sensitivity simulation, a point source with $100 \mu\text{Ci}$ activity was translated from the center of the FOV to the edges along the x , y , and z directions [see Fig. 1(a) for axes definition]. The true, random, scatter, and noise equivalent count (NEC) rates were determined using a simulated breast tissue phantom which fills the entire space between the two camera panels for 4 and 8 cm panel separations. Noise-equivalent count (NEC) is calculated as²²

$$\text{NEC} = \frac{T^2}{T + S + 2R}, \quad (1)$$

where T , S , and R are rates of true, scatter, and random coincidence events. Activities in the simulated breast tissue were varied from $10 \mu\text{Ci}$ up to 2 mCi. In these simulations, the energy window was wide open (10 keV up to 1 MeV) and the coincidence time window used was 10 ns. Results with narrower energy and time window settings were determined in post-processing of the simulated event list. Energy resolution and coincidence time resolutions assumed in the

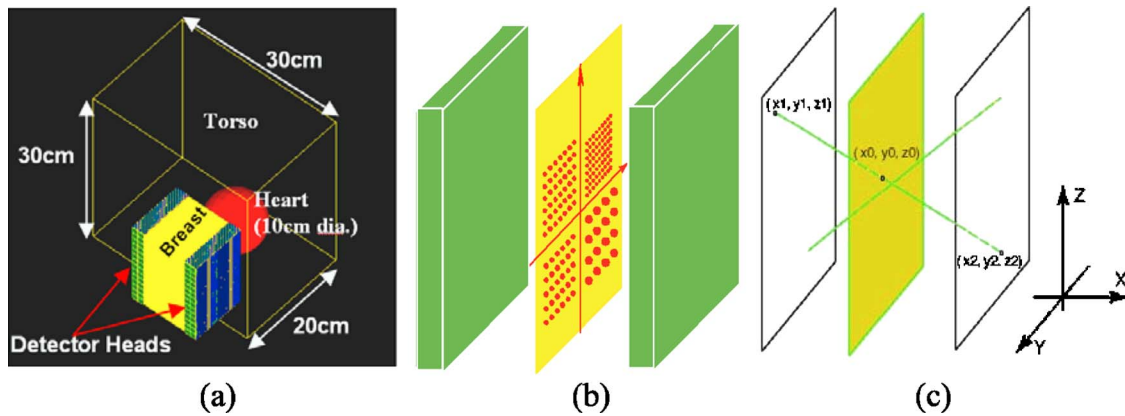


FIG. 2. (a) A dual-panel geometry PET camera with breast, heart (10 cm diameter) and torso background present, the plate separation is adjustable (4–8 cm was studied); (right) four quadrants of tumor spheres (2.5, 3, 3.5, and 4 mm diameter with twice the diameter separation) placed within simulated breast tissue that completely fills the space in between plates. (c) Schematic of the focal plane tomography algorithm used for reconstruction of the sphere plane.

simulations were 12% FWHM at 511 keV and 2 ns FWHM, respectively, which are the average measured energy and time resolutions from experiments.^{19,20}

For simulated count rate studies on the proposed dual-panel system, we included hot heart and warm torso compartments adjacent to the breast tissue compartment (Fig. 2(a)). Again, the breast tissue compartment completely filled the volume between the two simulated panels. Figure 2(a) depicts the geometry of the breast, heart, and torso compartments of the phantom as well as the detector system. The heart compartment was simulated as a 10 cm diameter sphere and the torso as a $30 \times 30 \times 20 \text{ cm}^3$ volume. To study lesion visualization capabilities a simulated tumor source plane placed within the breast tissue was included. This tumor source plane comprised spheres with four different diameters (2.5, 3, 3.5, and 4 mm) placed in a separate quadrant, and distributed with a separation of two times the diameter, as shown in Fig. 2(b). For most of the sphere image data presented, the activity concentration ratio simulated for tumor:breast:heart:torso was 10:1:10:1, which is consistent with the literature for fluorodeoxyglucose (FDG) tracer uptake in breast cancer,^{23–25} however lower concentration ratios were also studied. Table I shows the absolute activities, activity concentrations and volumes of the simulated breast, heart and torso tissue for 4 and 8 cm panel separation (breast tissue thickness). For most of the lesion visualization simu-

TABLE I. Activity concentration in phantom tissue compartments and corresponding compartment volumes used in the simulated dual-panel PET data acquisitions for data with tumor:breast:heart:torso concentration ratios of 10:1:10:1.

Phantoms	Activity concentration ($\mu\text{Ci}/\text{cm}^3$) (Refs. 23–25)	Volume (cm^3)	Activities (μCi)
Breast	0.1	$8 \times 15 \times 10 = 1200$	120
		$4 \times 15 \times 10 = 600$	60
heart	1	523.6	523.6
Torso	0.1	$30 \times 30 \times 20 = 18000$	1800

lation data presented the tumor source plane was placed midway between the two panels, however, we also studied locations offset from the center as well.

For a comparison to the lesion visualization capabilities for a dual-panel PET system that uses larger crystal pixel size, we simulated two $10 \times 15 \text{ cm}^2$ panels comprising LSO crystals of $2 \times 2 \times 10 \text{ mm}^3$ with no DOI resolution, $3 \times 3 \times 30 \text{ mm}^3$ with 10 mm DOI resolution, and $4 \times 4 \times 20 \text{ mm}^3$ with no DOI resolution, in addition to the proposed $1 \times 1 \times 3 \text{ mm}^3$ crystal design. The first three crystal sizes correspond to that used in existing dedicated breast^{3–7} and whole-body PET system designs.¹⁷ Thus, these simulations modeled the overall same panel dimensions, but with different crystal parameters. All of the simulation parameters for different crystals are summarized in Table II. The different energy resolutions achieved with these designs^{3–7,17} are determined by the detector design (crystal pixel size, photodetector, etc.) used. Although the dual-panel PET camera was simulated with different crystal resolution and energy resolution values, the coincidence time resolution was fixed at 2 ns FWHM to isolate the combined effects of spatial and energy resolutions on lesion visualization. In reality the other PET breast imaging solutions^{3–7,17} also had worse than 2 ns coincidence time resolution and thus random background contamination would increase, which would further degrade image contrast.

To further evaluate the camera lesion visualization performance, we simulated different source to background activity concentration ratios of 5:1 and 3:1, and also performed simulations with the tumor source plane at 1 cm offset from the center plane with 4 cm panel separation.

For image reconstruction, focal plane tomography (FPT)⁶ was employed. The FPT algorithm estimates the photon emission location by back projecting the lines of response (LOR) formed by the recorded interaction coordinates in the left and right panels through a set of image planes parallel to the two panels. The image plane may be placed anywhere between the two detector panels, but the resolution is the best at the foci of the LORs. The image plane where the LORs

TABLE II. Parameters used in Monte Carlo simulations to study sphere visualization capabilities for different crystal resolutions using 15×10 cm² panels.

LSO crystal size (mm ³)	$1 \times 1 \times 3$	$2 \times 2 \times 10$ (Ref. 3)	$3 \times 3 \times 30$ (Refs. 4 and 5)	$4 \times 4 \times 20$ (Ref. 17)
Effective crystal thickness (mm)	18 (six layers)	10	30	20
Energy resolution at 511 keV (% FWHM)	12%	16%	25%	20%
Energy window (keV)	450–573	350–650	350–650	350–650
Coincidence time resolution (ns, FWHM)	2	2	2	2
Coincidence time window (ns)	4	4	4	4
DOI resolution (mm FWHM)	3	10	10	20

focus is considered to be the best estimation of a focal emission source location. As shown in Fig. 2(c), the left (x_1, y_1, z_1) and right (x_2, y_2, z_2) interaction positions in the panels determine the LOR. The ability to provide the 3D interaction coordinates is possible due to the 3 mm interaction depth resolution resulting from the crystal layers in our detector design. When we backproject the data using the FPT algorithm, instead of backprojecting from the front surface of a single crystal, we backproject from the 3D interaction coordinate. In the data shown in this paper, this 3D interaction coordinate was defined by the center of the crystal that is closest to the true photon interaction position. Note that this DOI positioning significantly increases the number of backprojected lines in the FPT algorithm to effectively improve sampling in addition to reducing DOI parallax error.

The set of interception points (x_0, y_0, z_0) of the back projected LORs on the image plane generates the focal plane image parallel to the y - z plane at $x=x_0$ (Fig. 2(c)). Tissue attenuation as well as crystal attenuation and solid-angle (i.e., normalization) corrections were implemented in the image reconstruction. The tissue phantom is filled with water in the simulations and thus the attenuation coefficient of water was used (0.095 cm^{-1} at 511 keV) to calculate tissue attenuation correction factors for each LOR. As part of the normalization process, the solid angle subtended at the crystal surfaces by the focus of the LORs was calculated and corrected for each LOR. Crystal intrinsic detection efficiency factors for each LOR were determined using the known attenuation coefficient of LSO for 511 keV photons (0.869 cm^{-1}) and angle of entrance. A combined correction image was formed by taking the inverse of the back projection of every LOR pair between the two panels onto the focal plane. Tissue attenuation and normalization corrections were implemented by multiplying the reconstructed image with the correction image. To reduce aliasing artifacts, dithering of the binning coordinates was used to accurately model the volume element of each detector.

III. RESULTS

A. Point source coincidence photon sensitivity

Simulated photon sensitivity versus coincidence time and energy window settings are plotted in Fig. 3 with a point

source ($100 \mu\text{Ci}$ activity) at the center of the FOV for 4 and 8 cm panel separations (left and right column, respectively). The photon sensitivity (%) was plotted versus the coincidence time window at different energy windows centered on 511 keV [Figs. 3(a) and 3(b)], and versus energy window at different coincidence time windows [Figs. 3(c) and 3(d)]. For both panel separations of 4 and 8 cm, a sensitivity plateau was reached at a time window of around 3 to 4 ns [Figs. 3(a) and 3(b)]. For example, for an energy window of 350–650 keV, the photon sensitivity plateaus were at 14.2% and 8.2%, respectively, for the 4 and 8 cm plate separation. Figures 3(c) and 3(d) show that a sensitivity plateau was first reached at a energy window of about 25–30% centered on 511 keV, corresponding to an energy range of about 447–575 keV (25%) to 434–587 keV (30%). Thereafter, the photon sensitivity begins to increase again at an energy window setting of around 65%. This slope change is due to the fact that the further enlarged energy window includes more low energy scatter events from the energy spectrum. An advantage of the excellent energy resolution achieved ($\leq 12\%$ FWHM at 511 keV) is that a narrow energy window setting around 511 keV (e.g., 450–575 keV) can be used for photon scatter reduction, while still achieving high photon sensitivity.

To evaluate the photon sensitivity as a function of position, we moved the point source ($100 \mu\text{Ci}$ activity) along the x , y , and z axes [see Fig. 1(a)] with a step size of 1 cm. The calculated photon sensitivity versus position was plotted in Fig. 4 with the panel separation of 4 cm [Figs. 4(a)–4(c)] and 8 cm [Figs. 4(d)–4(f)]. Note that by reducing the panel separation from 8 to 4 cm, the average point source photon sensitivity was increased by about 80%.

B. Coincidence count rate studies

Figure 5 shows the true, scatter, random, total and NEC rates, calculated using Eq. (1), as a function of the activity in the breast (lower x -axis) and heart compartment (upper x -axis) with panel separation of 4 and 8 cm and 4 ns time window and $\sim 24\%$ energy window. Background activity from heart and torso were included in these simulations. The peak NEC with 4 cm panel separation was

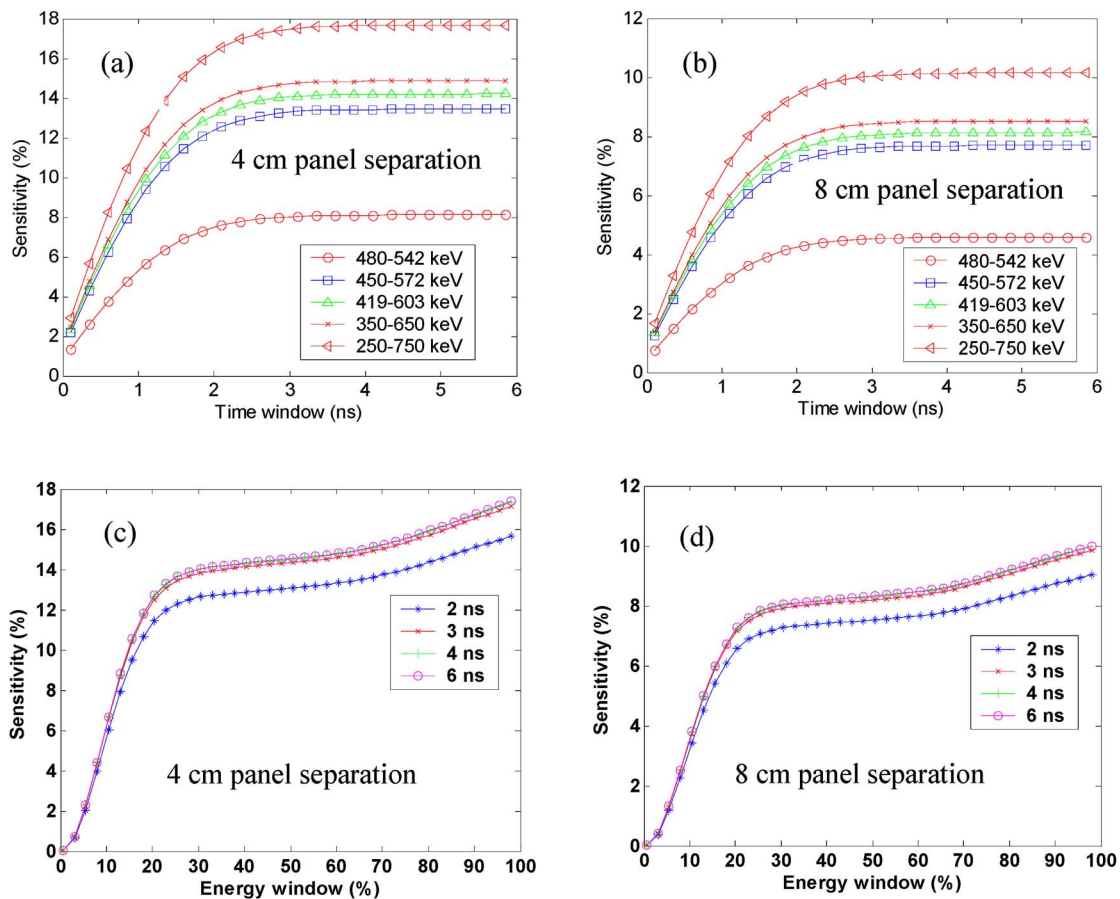


FIG. 3. Center point source ($100 \mu\text{Ci}$) sensitivity as a function of (a) and (b) coincidence time window for different energy windows and (c) and (d) versus energy window for different coincidence time windows for panel separation of 4 cm [(a) and (c)] and 8 cm [(b) and (d)].

$\sim 25\,000$ counts/s with $\sim 100 \mu\text{Ci}$ in the breast tissue compartment [Fig. 5(a)]. A plot of the NEC versus coincidence time window for different energy windows and as a function of energy window for different time windows with $100 \mu\text{Ci}$ activity in the breast compartment is presented in Fig. 6, with panel separation of 4 cm. Due to significantly higher random events for the particular breast, heart and torso activity distributions studied, the NEC peaks at 2.2 ns time window (about the coincidence time resolution) rather than 4 ns ($=2 \times$ coincidence time resolution), which is where the total system photon sensitivity plateaus (Fig. 4). With consideration of obtaining high photon sensitivity for breast tissue completely filling two panels separated by 4–8 cm, the 4 ns time and 24% energy windows settings were used in the processing of the simulated tumor data acquired with the dual-panel camera based on $1 \times 1 \times 3 \text{ mm}^3$ LSO crystals presented in the next section.

C. Small sphere visualization study

Figure 7 shows focal plane tomography (FPT) reconstructed images from simulated data of 2.5, 3, 3.5, and 4 cm diameter spheres in cold water acquired with dual-panel systems of different crystal pixel size without any background activity in the breast, heart or thorax compartments present.

As described in Sec. II, the simulated four dual-panel systems had crystal resolutions of (a) $1 \times 1 \times 3 \text{ mm}^3$ with 3 mm FWHM DOI resolution, (b) $2 \times 2 \times 10 \text{ mm}^3$ no DOI resolution, (c) $3 \times 3 \times 30 \text{ mm}^3$ with 10 mm FWHM DOI resolution, and (d) $4 \times 4 \times 20 \text{ mm}^3$ with no DOI resolution. These crystal sizes correspond to existing breast dedicated and whole-body PET system designs.^{3–5,17} Activity concentration in the sphere sources was $1 \mu\text{Ci}/\text{cc}$. In this “ideal” tracer uptake case (no background activity present), Fig. 7 clearly illustrates the effect of crystal resolution on small sphere visualization. Figure 7 images also give a sphere visualization “gold standard” to compare to for simulated data that includes breast tissue and out of FOV heart and torso background activity.

Figures 8(a)–8(d) shows FPT reconstructed images with only breast tissue activity present as background and the sphere:breast activity concentration ratio is 10:1. The 1D profiles taken through the sources along the lines marked by the arrows in Fig. 8(a) were plotted in Figs. 8(e) and 8(f). The contrast [Fig. 8(g)] and peak-to-valley ratio [Fig. 8(h)] were calculated and plotted in Figs. 8(g) and 8(h). The contrast is defined here as

$$\text{Contrast} = \frac{\max(\text{signal}) - \text{mean}(\text{bkgd})}{\max(\text{signal})}, \quad (2)$$

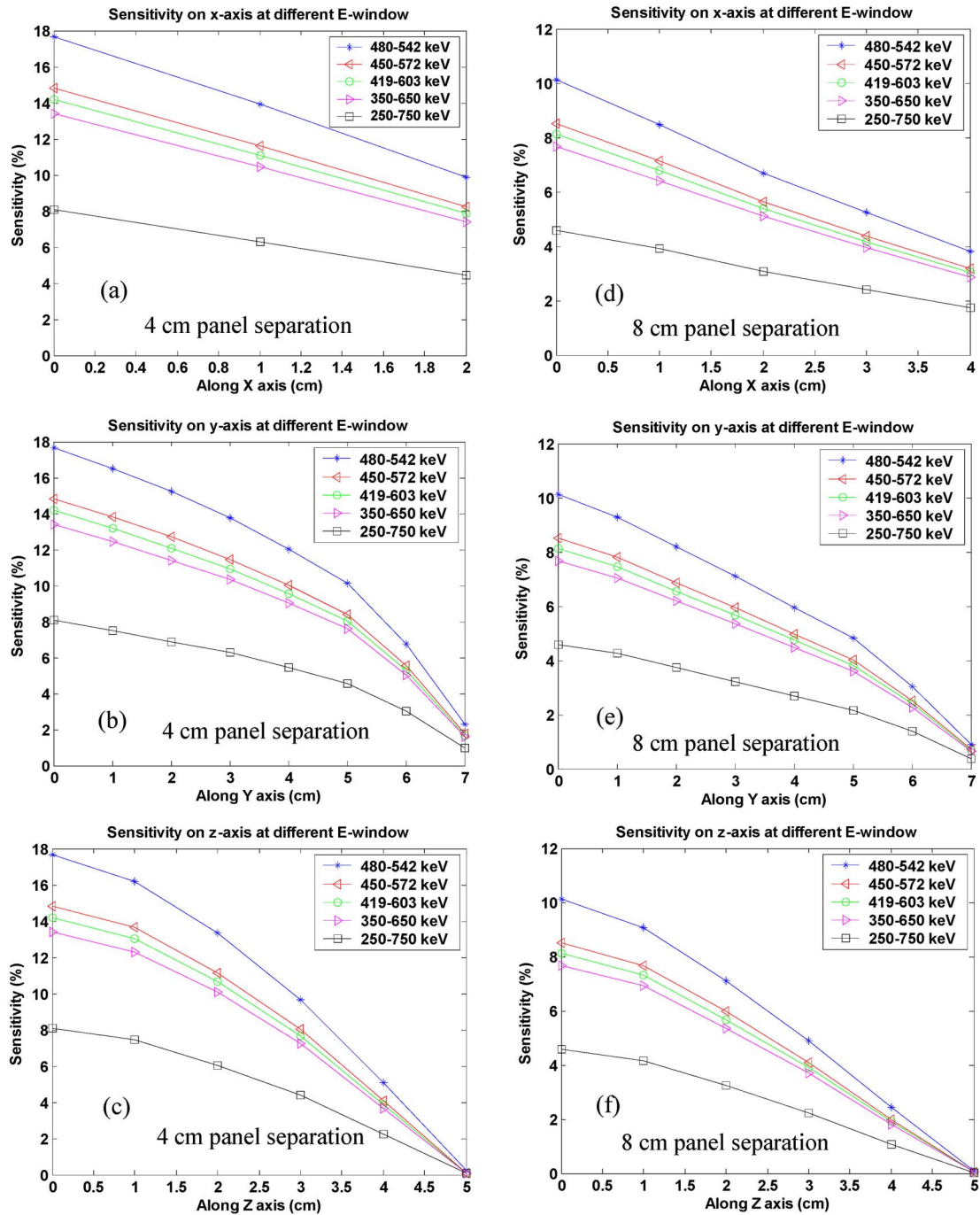


FIG. 4. Sensitivity for a point source ($100 \mu\text{Ci}$) translated from the center to the edge along the x , y , and z axes with panel separation of 4 cm (a), (b), (c), and 8 cm (d), (e), and (f) for different energy windows at 4 ns time window. (See Fig. 2(a) for axes definitions).

where the $\max(\text{signal})$ is maximum count within a 5×5 -pixel ROI centered at a sphere source, and the $\text{mean}(\text{bkgd})$ is the average background counts calculated from an ROI (e.g., row 295:305 column 345:355 at the right side of the image), where no sphere sources were located. The peak to valley ratio was simply calculated as the ratio of the maximum value at the source location to the minimum value at the valley location between two same size sphere sources from the 1D profile plots. All curves were normalized by the

central pixel count for easy comparison. The data and error bars were calculated based on two sources at each diameter. Figure 8 illustrates how breast tissue background alone effects sphere visualization.

Images corresponding to data acquired with breast, heart and torso background activity present (10:1:10:1 concentration ratio) are shown in Figs. 9(a)–9(d) together with the 1D profiles along the rows marked with arrows in Fig. 9(a). The contrast and peak-to-valley ratio are also plotted in Figs. 9(g)

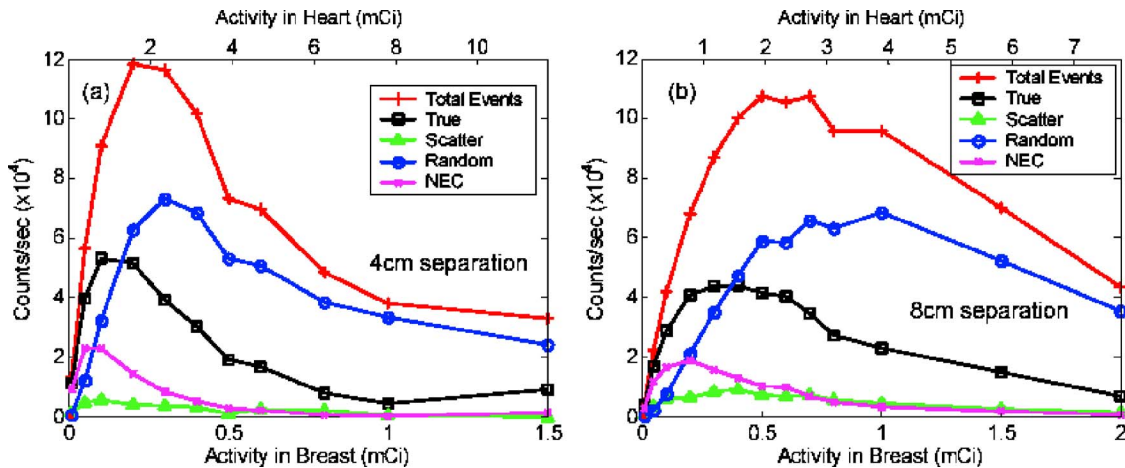


FIG. 5. True, random, scatter, totals (T+S+R), and NEC rates as a function of the activity in breast with panel separation of (a) 4 cm and (b) 8 cm. Energy and coincidence time window settings used for the plots were 24% (450–572 keV) and 4 ns, respectively.

and 9(h). Please note that the acquisition time of the data reconstructed in Figs. 8 and 9 are all only 30 s with around 2 million counts in each image. The high photon sensitivity facilitated by close-proximity and thick panels allows these short acquisition times.

To understand the sphere resolution capability of the dual-panel system for spheres located offset from the central plane, we also performed the simulation with the source plane at a 1 cm offset position from the center between the two detector panels separated by 4 cm for the camera system based on the $1 \times 1 \times 3$ mm³ LSO crystals. Background breast tissue activity is present with a sphere:breast concentration ratio of 10:1. The reconstructed result is shown in Fig. 10(a). Figures 10(b) and 10(c) show 1D profiles through the spheres indicated by the arrows for this offset as well as for data with the tumor plane at the center [Fig. 8(a)]. Figure 10(d) shows reconstructed data for spheres located at the center plane with a panel separation of 8 cm with warm breast, heart and torso present (same activity concentration ratio as Fig. 9(a) sphere:breast:heart:torso=10:1:10:1). Fig-

ures 10(e) and 10(f) show 1D profiles through the spheres indicated by the arrows for this as well as for the 4 cm panel separation data [Fig. 9(a)].

To evaluate the effect of activity ratio on the sphere visualization, we also studied lower simulated tumor to breast activity concentration ratios of 5:1 and 3:1 corresponding to a less specific tracer. In this study, we used a source plane similar to those used in Figs. 8–10 but with the array of source spheres extended to the full FOV of the camera. The results are shown in Fig. 11 together with 1D profile plot along the arrow direction marked in Fig. 11(a). The contrast and peak-to-valley ratio were also plotted in Figs. 11(f) and 11(g). Note in the contrast calculation here, as the sources are distributed over the entire image plane, the background is calculated as the average counts of the center two rows between spheres in the images.

IV. DISCUSSION

A typical clinical PET system has >5 mm FWHM spatial resolution at the center that degrades with radial position,

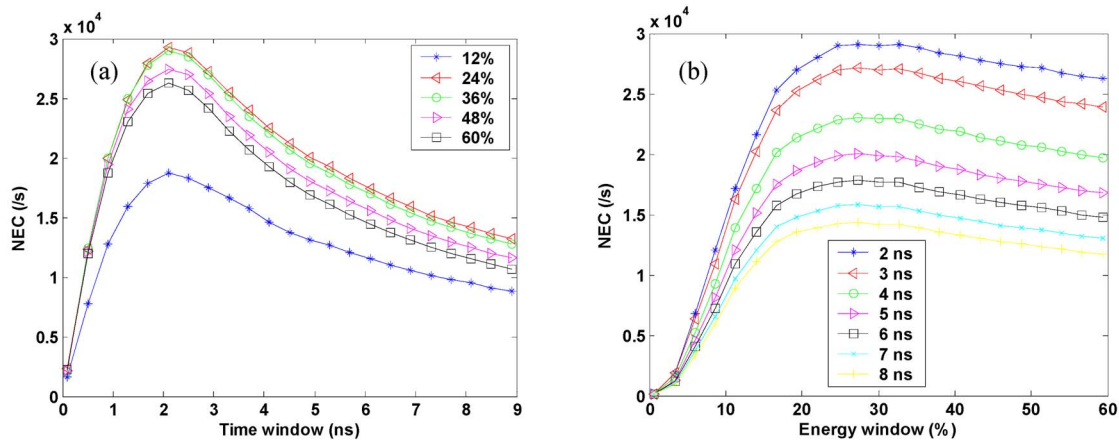


FIG. 6. Plot of NEC versus (a) coincidence time window for different energy windows centered at 511 keV and (b) energy window for different coincidence time windows with 100 μ Ci in the breast for 4 cm panel separation, with breast tissue completely filling the space between the two panels.

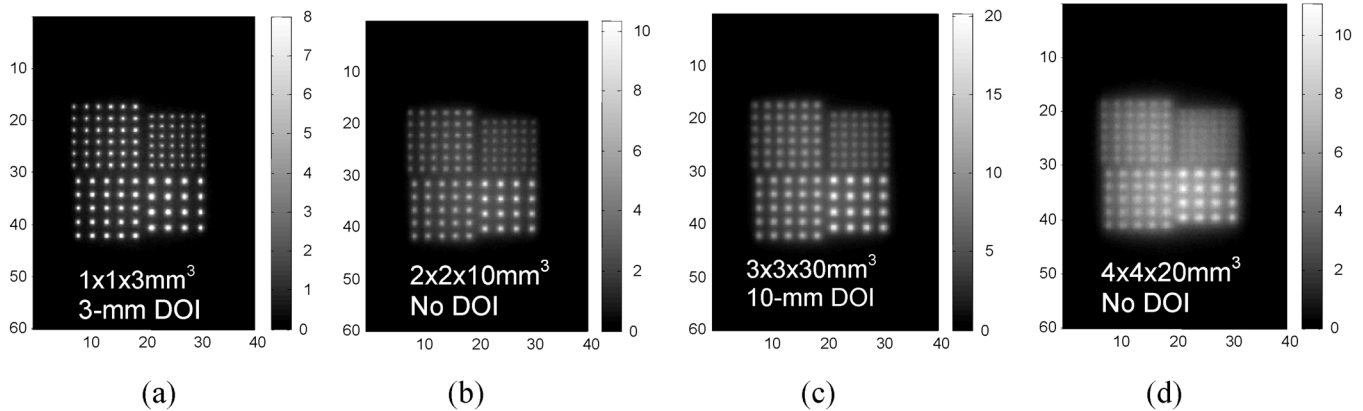


FIG. 7. Focal plane tomography reconstructions of the hot spheres acquired in $10 \times 15 \text{ cm}^2$ panels built with LSO crystal pixel dimensions of (a) $1 \times 1 \times 3 \text{ mm}^3$ with 3 mm FWHM DOI resolution, (b) $2 \times 2 \times 10 \text{ mm}^3$ without DOI resolution, (c) $3 \times 3 \times 30 \text{ mm}^3$ with 10 mm FWHM DOI resolution, and (d) $4 \times 4 \times 20 \text{ mm}^3$ without DOI resolution. (see Table II for resolutions and window settings). Sphere diameters are counter-clockwise from top right 2.5, 3.0, 3.5, and 4.0 mm with twice the separation.

$<1\%$ photon sensitivity, $>20\%$ FWHM energy resolution, and $>3 \text{ ns}$ FWHM coincidence time resolution.¹⁷ This performance, together with the large and awkward geometry, and high cost makes the standard clinical PET system not optimal for breast cancer imaging. The system proposed is built from modules comprising of 1 mm LSO crystals coupled to novel, extremely thin, flex-circuit mounted PSAPDs. Measurements with these detectors have achieved on average $\leq 12\%$ FWHM energy resolution at 511 keV, $\sim 2 \text{ ns}$ FWHM coincidence time resolution, and $\sim 1 \text{ mm}$ intrinsic spatial resolution.^{19,20} Based on this detector performance, we have used Monte Carlo simulation to study the performance (the photon sensitivity, count rate, and lesion visualization capabilities) of a dual-panel breast-dedicated PET system using GATE open-source software.²¹

In the lesion visualization simulations, a fixed 2 ns FWHM coincidence time resolution (Table II) was used for the study of properties of panel systems of different crystal and energy resolutions that have been achieved in other cameras used for breast imaging.^{3-7,17} In practice, the other crystal resolution designs do not achieve the 2 ns time resolution, and worse random coincidence background effects would be expected.

Figures 7–9 show that for the $1 \times 1 \times 3 \text{ mm}^3$ LSO based PET camera, the small spheres are better visualized (brighter, smaller, and better separated), the contrast and peak (lesion) to background ratio are markedly superior [see Figs. 8(g) and 8(h) and Figs. 9(g) and 9(h)], and the background gradient from the nearby hot heart compartment (left to right) is lower than the other systems with larger crystal size and worse energy resolution. Thus, the improved spatial and energy resolutions help to significantly enhance lesion visualization capabilities. For example, for the 4 mm diameter sources in Fig. 8, the contrast is 0.55 for the 1 mm crystal data compared to 0.37, 0.33 and 0.27 for the $2 \times 2 \times 10 \text{ mm}^3$, $3 \times 3 \times 30 \text{ mm}^3$, $4 \times 4 \times 20 \text{ mm}^3$ crystal resolutions, respectively [Fig. 8(g)]. For the 4 mm diameter sources, the mean peak-to-valley ratio is 1.96 for the 1 mm crystal data compared to

1.22, 1.22 and 1.16 for the $2 \times 2 \times 10 \text{ mm}^3$, $3 \times 3 \times 30 \text{ mm}^3$, $4 \times 4 \times 20 \text{ mm}^3$ crystal resolutions, respectively [Fig. 8(h)]. Similar results were observed in Figs. 9(g) and 9(h). Please notice that in Fig. 9(g), the contrast values of 3.5 and 3 mm sources were relatively higher than that of the 4 mm sources for $2 \times 2 \times 10 \text{ mm}^3$, $3 \times 3 \times 30 \text{ mm}^3$, $4 \times 4 \times 20 \text{ mm}^3$ crystal resolutions. This reason for this is that the 3.5 and 3 mm sources are closer to the heart and torso background and the $\max(\text{signal})$ included contributions from that substantial background.

As also shown in the images in Figs. 7–9, the superior intrinsic spatial resolution (1 mm in plane, 3 mm DOI) leads to tumor foci appearing brighter, narrower and better separated. The superior energy resolution (12% FWHM at 511 keV) combined with better spatial resolution leads to superior reconstructed tumor to background contrast, especially in the presence of strong background from the adjacent heart and torso [Figs. 9(a)–9(d)]. With excellent energy resolution ($<12\%$ FWHM at 511 keV) one can use narrow energy window (e.g., 24%) to significantly reduce the scatter and random coincidence background events without degrading statistical quality of the data; Random events are also reduced with a narrow energy window setting since many of the single photon events also undergo scatter.

Figure 10(a) presents the simulation data with the source plane at 1 cm offset from the central plane between the two detector panels separated by 4 cm. It is noticed that using focal plane tomography for image reconstruction, with the sources located at an offset position from the center of the FOV, the spatial resolution is degraded. Figures 10(b) and 10(c) plot the 1D profile through spheres in Fig. 10(a) together with the profiles through same spheres from Fig. 8(a) for comparison. To evaluate the spatial resolution degradation going off-center, triangle fitting was applied to the 3.5 mm sphere profile curves with background activity offset correction. Moving from the center to 1 cm offset planes, the average FWHM of the fitted curves increased from 2.4 mm to 3.0 mm FWHM. Thus, the best resolution of this camera

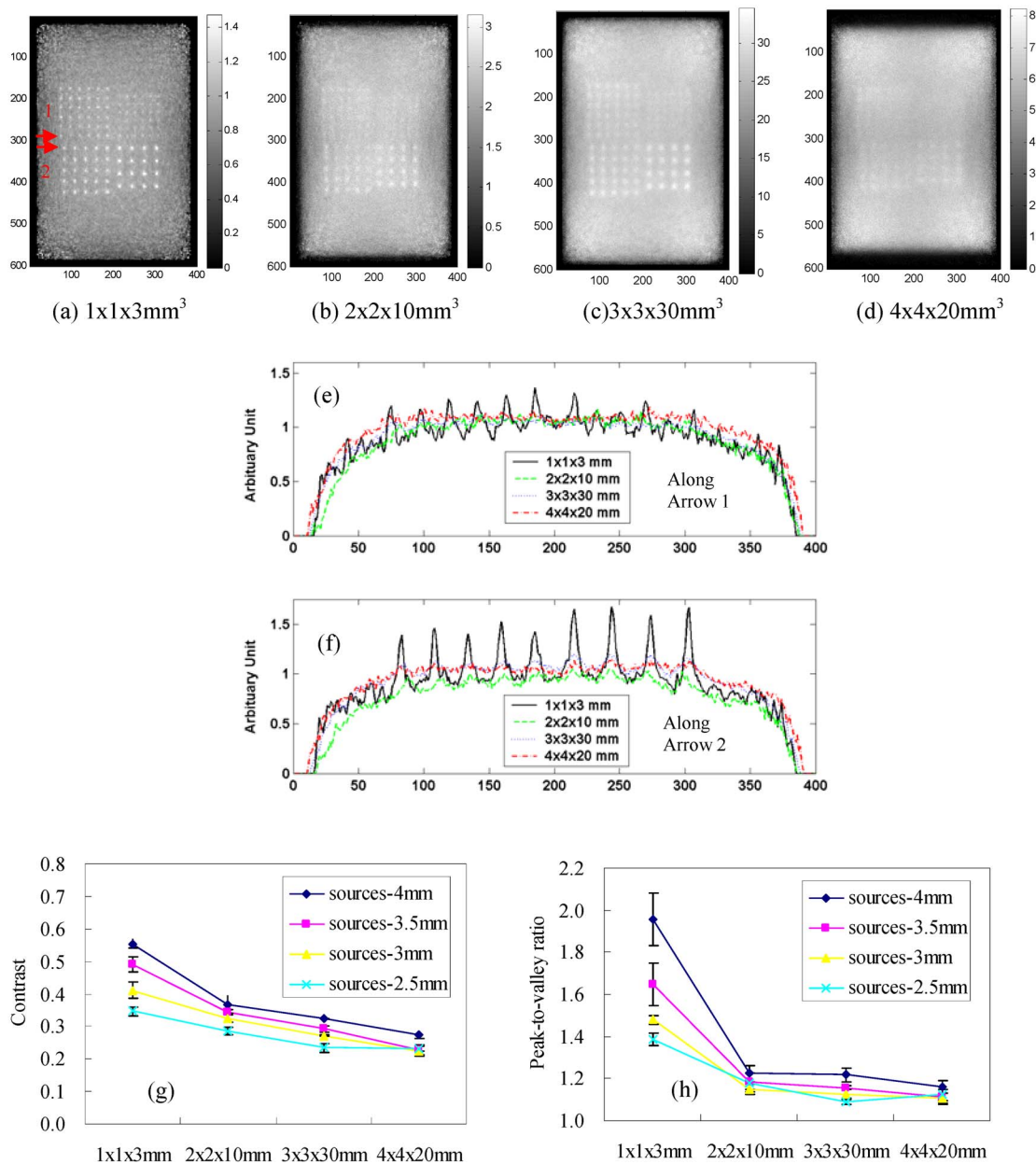


FIG. 8. (a)–(d) Focal plane tomography image reconstructions of data acquired for 30 s, with hot tumors in center plane, warm breast tissue background (10:1 tumor to background activity concentration ratio), and 4 cm plate separation for different LSO crystals pixel dimensions, DOI resolution and energy resolution. Images are reconstructed with normalization and photon tissue attenuation corrections. (e) Plots of 1D profiles taken through the bottom row of the 3.0 and 2.5 mm spheres in the images (each normalized by the central pixel counts), and (f) through the top row of the 3.5 and 4.0 mm diameter spheres as indicated by the arrows in the image in (a); (g) contrast and (h) peak-to-valley ratio versus crystal size for different sphere diameters (see Table II for resolutions and window settings).

is at the center of the camera plane. Note that these reconstructed FWHM values (~ 2.4 mm at center and 3.0 mm at 1 cm offset) are a convolution of the intrinsic spatial resolution with the FWHM of the projected profile of the 3.5 mm diameter spherical source distribution.

Figure 10(d) shows a sphere source image acquired with the panel separation of 8 cm at tumor:breast:heart:torso activity concentration ratios of 10:1:10:1. As the photon sensitivity and spatial resolution drop significantly with panel distance of 8 cm (see sensitivity comparison in Fig. 4), the lesion visualization capabilities (e.g., peak-valley ratios and sphere-to-background contrast) degrade, as shown in the 1D

profiles plotted in Figs. 10(e) and 10(f), compared to the data acquired with 4 cm separation [Fig. 9(a)]. At 8 cm panel separation the 2.5 mm diameter spheres are basically no longer visible.

As different patients, tissues, and tumor phenotype will exhibit a wide range of tumor:background uptake ratios for a given tracer, it is important to understand how this will effect lesion visualization. Figure 11 shows results from simulations of three different activity concentration ratios of 10:1 [Fig. 11(a)], 5:1 [Fig. 11(b)], and 3:1 [Fig. 11(c)] with only breast background present and 4 cm panel separation. By

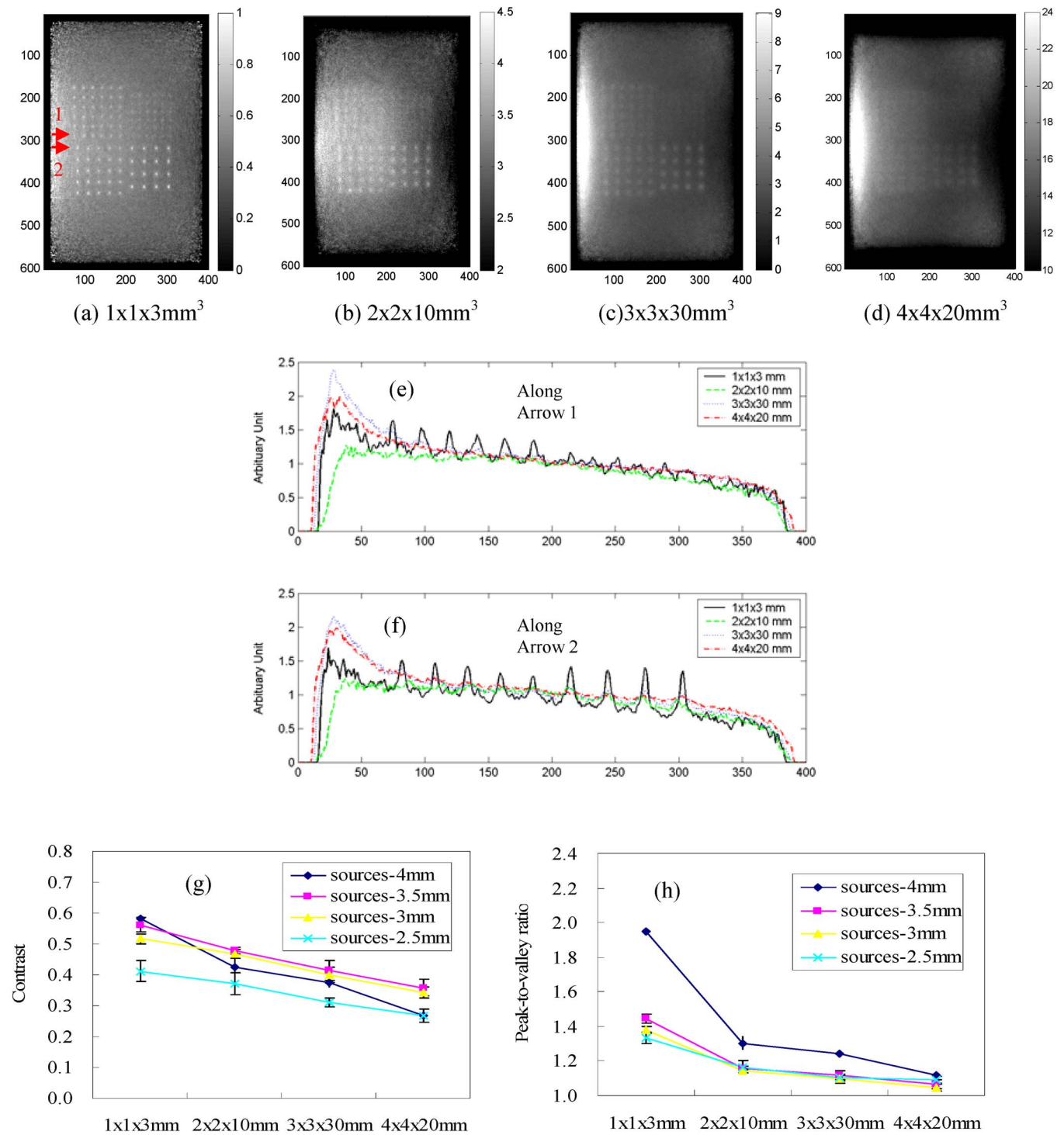


Fig. 9. (a)–(d) Images after only 30 s data acquisition with tumor:breast:heart:torso activity ratio of 10:1:10:1, with 4 cm plate separation for different LSO crystal pixel size (see Table I for details). The activity gradient seen from the left to the right edge of the images is due to high background activity from the simulated heart (see Fig. 2(a)). (e) Plots of 1D profiles taken through the bottom row of the 3.0 and 2.5 mm spheres, and (f) through the top row of the 3.5 and 4.0 mm diameter spheres as indicated by the arrows in the image in (a); (g) contrast and (h) peak-to-valley ratio versus crystals size for different sphere diameters.

comparing the 1D profiles through the sphere sources indicated by the arrows in the image of Fig. 11(a), we see that the reduction of tumor:background activity ratio produces a significant decrease in the sphere contrast and peak to value ratio values (Figs. 11(f) and 11(g)). Therefore, the develop-

ment of tracers with higher specificity to breast cancer will substantially improve the lesion visualization capabilities of this method.

The photon sensitivity of this dedicated PET camera is also significantly higher than the standard whole body clini-

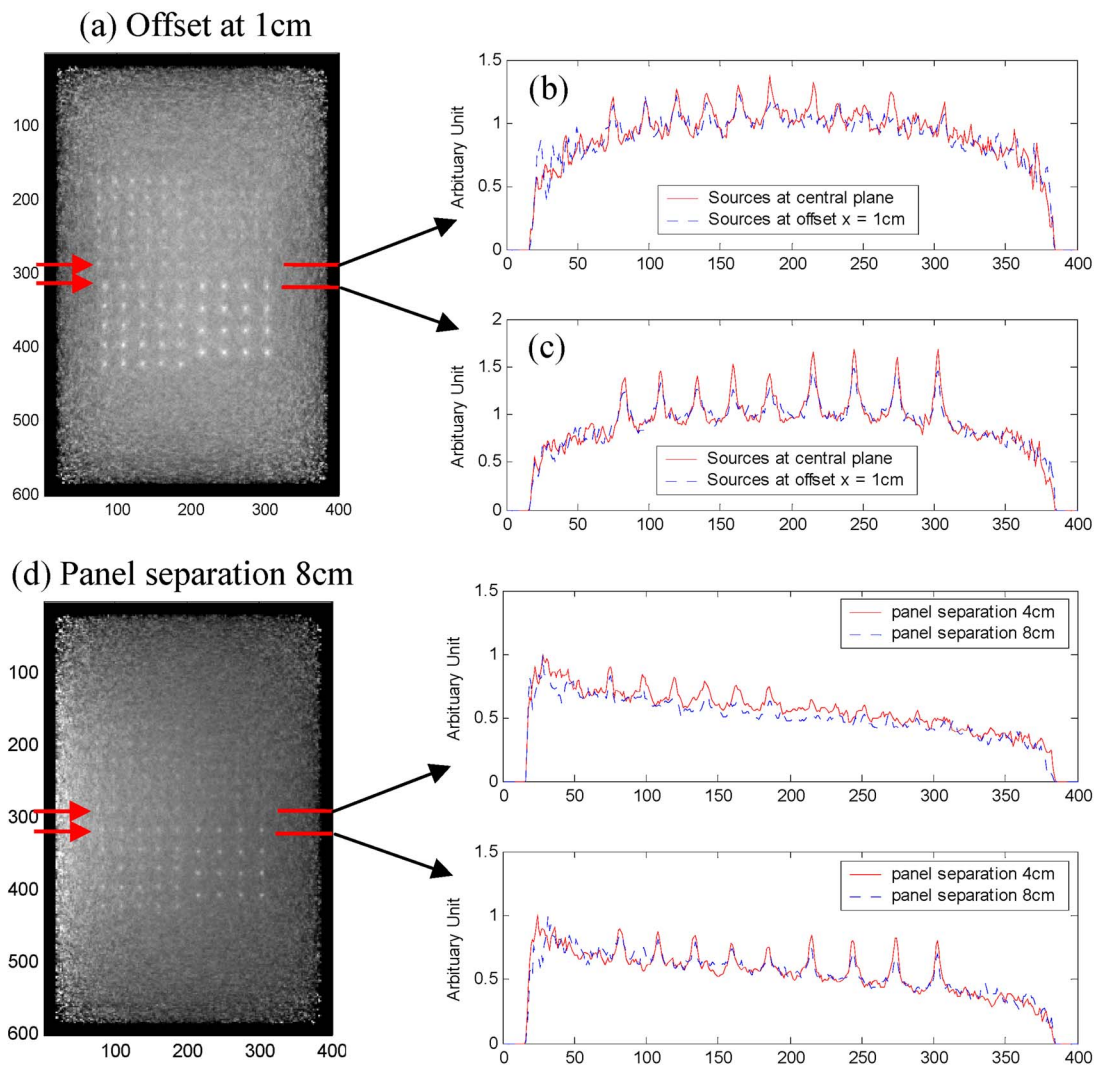


FIG. 10. (a) Reconstructed images of hot spheres resulting from data acquired in 1 mm crystal panel system with breast tissue as background with tumor: breast activity concentration ratio of 10:1 and hot sphere source plane offset at $x=1$ cm from the center for 4 cm panel separation; (b) and (c) 1D profile along arrows in (a) plotted together with the corresponding profile for the same spheres located at $x=0$ [data extracted from Figs. 8(e) and 8(f) data]. (d) With background activity of tumor:breast:heart:torso=10:1:10:1 with panel separation of 8 cm and hot sphere source plane located at $x=0$; (e) and (f) 1D profile along arrows in (d) plotted together with the profile through the same spheres for data acquired with panel separation of 4 cm [extracted from Figs. 9(e) and 9(f) data]. Profiles shown were taken through the images of the bottom row of the 2.5 and 3.0 mm diameter spheres and through the top row of the 3.5 mm and 4.0 mm diameter spheres.

cal system. At the center of the FOV, the proposed dual-panel camera with 4 cm panel separation has sensitivity of $\sim 14\%$ with a 350–650 keV energy window and 4 ns time window setting [see Fig. 3(a)]. This substantially improved photon sensitivity, helps to enhance the lesion visualization capabilities of the camera by facilitating good signal-to-noise ratio for high resolution image reconstructions. Because of the excellent photon sensitivity (see Fig. 3) the dual-plate system comprising $1 \times 1 \times 3 \text{ mm}^3$ crystals can resolve 2.5 mm diameter ($8 \mu\text{l}$) simulated tumor spheres in only 30 s acquisition time. Assuming these results will hold for the real system, this would reflect markedly improved capability compared to existing clinical systems.

The clinical pertinence of detecting a 2.5 mm diameter tumor, depends upon the clinical role the camera plays,

which is to be determined once the camera is built. However, we hypothesize the following impact of this improved PET lesion resolving power for various indications: If the role is to help with inconclusive mammograms ($\sim 25\%$ of all cases), please note that detecting lesions earlier (e.g., when they are smaller) improves prognosis for breast cancer. This fact is a main reason why mammography has played such an important role in breast cancer management. If it turns out that the camera can aid in diagnosis, visualizing smaller aggregates of biologically active malignant cells in a warm activity of background can help to guide or reduce the invasiveness of biopsy procedures by improving accuracy of sampling malignant tissue. If the role of the camera is helping to guide a breast cancer surgeon in removing the primary tumor, then visualizing smaller clumps of malignant tissue at

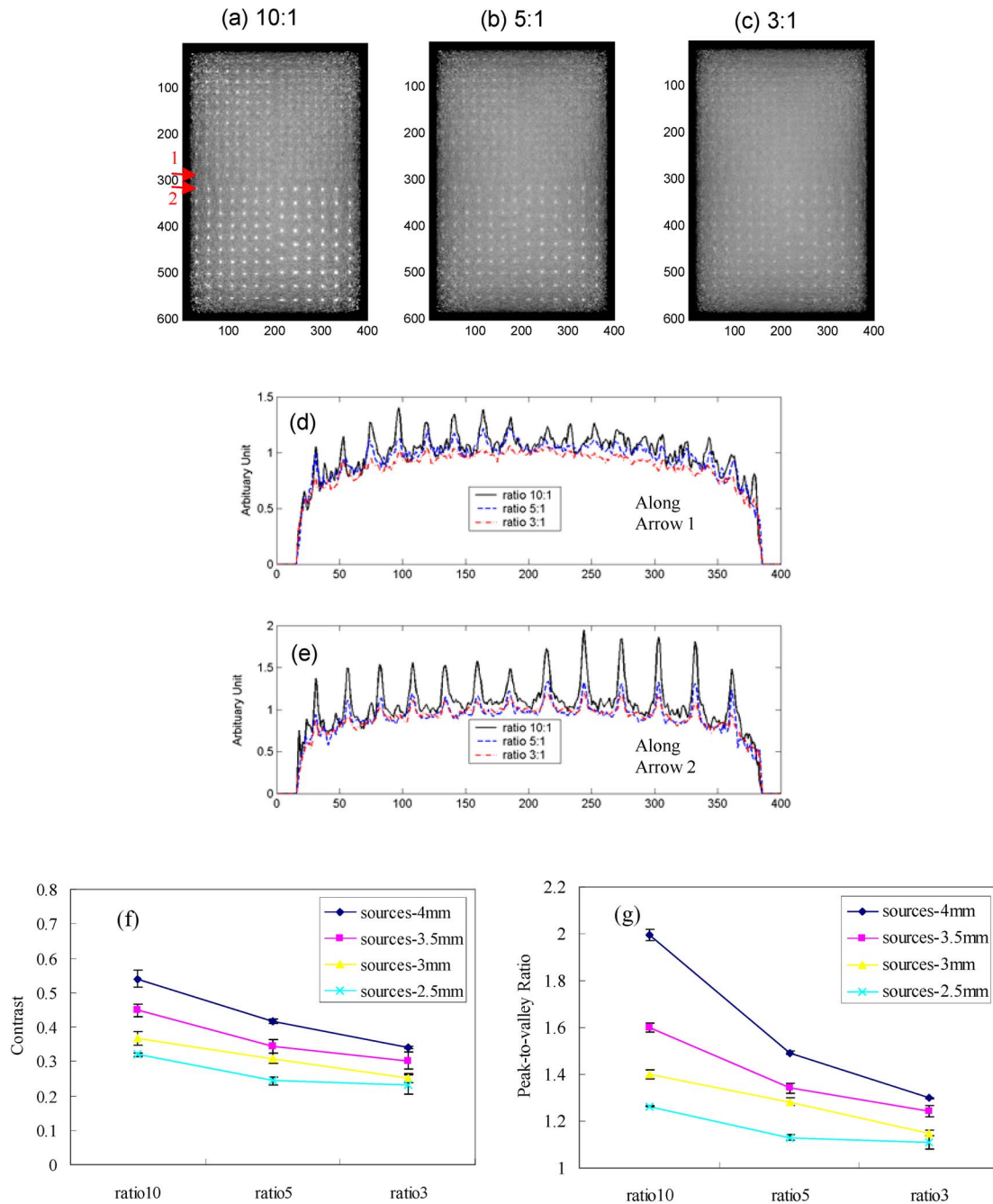


FIG. 11. Reconstructed images of hot spheres resulting from data acquired in 1 mm crystal panel system with breast tissue as background with tumor:breast activity concentration ratios of (a) 10:1, (b) 5:1, and (c) 3:1 and hot sphere source plane at the center plane ($x=0$). (d) and (e), 1D profile plots through spheres along the row marked by the arrows in the images (bottom row of the 2.5 and 3.0 mm diameter spheres and through the top row of the 3.5 mm and 4.0 mm diameter spheres). (f) Contrast and (g) peak-to-valley ratio versus tumor:breast activity ratio. Note for this study the sphere sources in the phantom extended all the way out to the FOV edge.

the resection margins could possibly help to reduce the rate of recurrence. The ability to detect smaller concentrations of PET tracer could also possibly help to visualize cancer cells as they start to accumulate in nearby lymph nodes, and hence help with accuracy of staging breast cancer. Finally, early visualization of miniscule focal accumulation of tracer could help the accuracy of identifying local recurrence.

A short acquisition time of 30 s could potentially help to increase PET's role in breast cancer management by simply

making it more practical to perform PET studies in the setting of a breast imaging clinic. Longer acquisition time affects patient comfort, especially if the breast is compressed, and decreases patient throughput. These are factors that currently make PET not as practical for the breast clinic. We envision that the proposed compact device will actually sit in the breast imaging clinic, so scan time, throughput, as well as footprint are critical issues. Alternatively, if desired, the high photon sensitivity can be used to significantly reduce the

injected dose given to the patient and therefore reduce radiation dosage to the patient for the same statistical image quality level.

Short scan times, low tracer uptake ratio, wide panel separation, and off-center lesion locations are examples of effects that challenge the breast lesion detection capabilities for a PET system. However, our data supports the hypothesis that the proposed camera with superior spatial, energy, temporal resolutions and photon sensitivity would yield superior lesion visualization capabilities compared to existing technologies, regardless of the imaging condition challenges.

V. CONCLUSION

We are developing a dual-panel PET system dedicated to breast cancer imaging. The system incorporates a new scintillation detector concept comprising $1 \times 1 \times 3 \text{ mm}^3$ LSO crystals coupled to a novel semiconductor photodetector. Those detectors have achieved 1 mm intrinsic spatial resolution, 3 mm DOI resolution, $<12\%$ energy and 2 ns coincidence time resolutions in measurements. Simulations predict that if we are successful in translating these detector results to the proposed dual-panel system, the result will be a tool with superior lesion visualization capabilities compared to breast-PET imaging technologies currently available. The directly measured DOI resolution will allow uniform spatial resolution to be achieved within the closely spaced detector FOV. The excellent energy resolution allows one to use a narrow energy window setting (e.g., 24%) to significantly reduce both scatter and random coincidence background, in order to improve lesion contrast resolution, while still maintaining high $>10\%$ coincidence photon detection efficiency for high statistical quality of the data. The high photon sensitivity facilitates image reconstruction at the desired spatial resolution with a relatively short scan duration that is practical for the breast imaging clinic.

ACKNOWLEDGMENTS

We thank Dr. Frezghi Habte for useful discussions. This work was supported in part by Grant Nos. #R21 CA098691 and R01 CA119056 from NIH-NCI and UC Breast Cancer Research Program Grant No. 12IB-0092.

^{a)}Now with PerkinElmer Optoelectronics, Santa Clara, California 95054. Electronic mail: jin.zhang@perkinelmer.com

^{b)}Electronic mail: pdo@stanford.edu

^{c)}Electronic mail: gchinn@stanford.edu

^{d)}Also at Physics Department, University of California, San Diego, CA 92037. Electronic mail: afoudray@stanford.edu

^{e)}Electronic mail: cslevin@stanford.edu

¹C. J. Bains *et al.*, "Sensitivity and specificity of first screen mammography in the Canadian National Breast Screening Study; a preliminary report from 5 centers," *Radiology* **160**, 295–298 (1986).

²P. S. Conti *et al.*, "PET and [F-18]-FDG in oncology: A clinical update," *Nucl. Med. Biol.* **23** (6), 717–735 (1996).

³I. N. Weinberg, D. Beylin, V. Zavarzin, S. Yarnall, P. Y. Stepanov, E. Anashkin, D. Narayanan, S. Dolinsky, K. Lauckner, and L. P. Adler, "Positron emission mammography: High-resolution biochemical breast imaging," *Technol. Cancer Res. Treat.* **4** (1), 55–60 (2005).

⁴W. M. Moses and J. Qi, "Instrumentation optimization for positron emission mammography," *Nucl. Instrum. Methods Phys. Res. A* **527**, 76–82 (2004).

⁵J. Qi, C. Kuo, R. H. Huesman, G. J. Klein, W. M. Moses, and B. W. Reutter, "Comparison of Rectangular and Dual-Planar positron emission mammography scanners," *IEEE Trans. Nucl. Sci.* **49**, 2089–2096 (2004).

⁶N. K. Doshi, Y. Shao, R. W. Silverman, and S. R. Cherry, "Design and evaluation of an LSO PET detector for breast cancer imaging," *Med. Phys.* **27** (7), 1535–1543 (2000).

⁷R. R. Raylman, S. Majewski, R. Wojcik, A. G. Weisengerger, B. Kross, V. Popov, and H. A. Bishop, "The potential role of positron emission mammography for detection of breast cancer: A phantom study," *Med. Phys.* **27** (8), 1943–1954 (2000).

⁸R. R. Raylman, E. P. Ficaro, and R. L. Wahl, "Stereotactic coordinates from ECT sinograms for radionuclide-guided breast biopsy," *J. Nucl. Med.* **37** (9), 1562–1567 (1996).

⁹S. Klein, "Evaluation of palpable breast masses," *Am. Fam. Physician* **71** (9), 1731–1738 (2005).

¹⁰B. L. Daniel *et al.*, "An MRI-compatible semiautomated vacuum assisted breast biopsy system: Initial feasibility study," *J. Magn. Reson Imaging* **21** (5), 637–644 (2005).

¹¹A. Fenster *et al.*, "The use of three-dimensional ultrasound imaging in breast biopsy and prostate therapy," *Measurement* **36** (3-4), 245–256 (2004).

¹²H. I. Vargas *et al.*, "Diagnosis of palpable breast masses: Ultrasound-guided large core biopsy in a multidisciplinary setting," *Am. Surg.* **70** (10), 867–871 (2004).

¹³C. A. Piron *et al.*, "A hybrid breast biopsy system combining ultrasound and MRI," *IEEE Trans. Med. Imaging* **22** (9), 1100–1110 (2003).

¹⁴A. Soluri *et al.*, "(TC)-T-99M[13LEU] Bombes in and a new gamma camera, the imaging probe, are able to guide mammotome breast biopsy," *Anticancer Res.* **23** (3A), 2139–2142 (2003).

¹⁵M. S. Soo, J. A. Baker, and E. L. Rosen, "Sonographic detection and sonographically guided biopsy of breast microcalcifications," *Am. J. Roentgenol.* **180** (4), 941–948 (2003).

¹⁶A. Soluri *et al.*, "Mammothome breast cancer biopsy: Combined guided with X-ray stereotaxis and imaging probe," *Nucl. Instrum. Methods Phys. Res. A* **497** (1), 122–128 (2003).

¹⁷A. M. Alessio, P. E. Kinahan, P. M. Cheng, H. Vesselle, and J. S. Karp, "PET/CT scanner instrumentation, challenges, and solutions," *Radiol. Clin. North Am.* **42**, 1017–1032 (2004).

¹⁸C. S. Levin, "Design of a high-resolution and high-sensitivity scintillation crystal array for PET with nearly complete light collection," *IEEE Trans. Nucl. Sci.* **49**, 2236–2243 (2002).

¹⁹C. S. Levin, A. M. K. Foudray, P. D. Olcott, and F. Habte, "Investigation of position sensitive avalanche photodiodes for a new high-resolution PET detector design," *IEEE Trans. Nucl. Sci.* **51**, 805–810 (2004).

²⁰J. Zhang, A. M. K. Foudray, P. D. Olcott, R. Farrell, and C. S. Levin, "Performance characterization of a novel thin position-sensitive avalanche photodiode for high resolution positron emission tomography," in *Proc. 2005 IEEE Medical Imaging Conf. Rec.*, Puerto Rico, Oct. 2005.

²¹S. Jan *et al.*, "GATE: a simulation toolkit for PET and SPECT," *Phys. Med. Biol.* **49**, 4543–4561 (2004).

²²S. C. Strother, M. E. Casey, and E. J. Hoffman, "Measuring PET scanner sensitivity: Relating count rates to image signal-to-noise ratios using noise equivalent counts," *IEEE Trans. Nucl. Sci.* **37**, 783–788 (1990).

²³N. Avril, M. Menzel, J. Dose, M. Schelling, W. Weber, F. Jänicke, W. Nathrath, and M. Schwaiger, "Glucose metabolism of breast cancer assessed by ¹⁸F-FDG PET: Histologic and immunohistochemical tissue analysis," *J. Nucl. Med.* **42** (1), 9–16 (2001).

²⁴R. L. Wahl, R. L. Cody, G. D. Hutchins, and E. E. Mudgett, "Primary and metastatic breast carcinoma: Initial clinical evaluation with PET with the radiolabeled glucose analogue 2-[F-18]-fluoro-2-deoxy-D-glucose," *Radiology* **179**, 765–770 (1991).

²⁵K. Murthy, M. Aznar, C. J. Thompson, A. Loutfi, R. Lisbona, and J. H. Gagnon, "Results of preliminary clinical trials of the positron emission mammography system PEM-I: A dedicated breast imaging system producing glucose metabolic images using FDG," *J. Nucl. Med.* **41**, 1851–1858 (2000).